Density functional modeling and total scattering analysis of the atomic structure of a quaternary CaO-MgO-Al₂O₃-SiO₂ (CMAS) glass: Uncovering the local environment of calcium and magnesium

Kai Gong , ¹ V. Ongun Özçelik , ^{1,2} Kengran Yang, ¹ and Claire E. White ^{1,*}

¹Department of Civil and Environmental Engineering, Andlinger Center for Energy and the Environment,

Princeton University, Princeton, New Jersey 08544, USA

²Department of Chemistry and Biochemistry, Materials Science and Engineering Program,

University of California San Diego, La Jolla, California 92093, USA

(Received 20 July 2020; revised 5 October 2020; accepted 7 December 2020; published 11 January 2021)

Quaternary CaO-MgO-Al₂O₃-SiO₂ (CMAS) glasses are important constituents of the Earth's lower crust and mantle, and they also have important industrial applications such as in metallurgical processes, concrete production, and emerging low-CO₂ cement technologies. In particular, these applications rely heavily on the composition-structure-reactivity relationships for CMAS glasses, which are not yet well established. In this study, we combined force-field molecular dynamics (MD) simulations and density functional theory (DFT) calculations to generate detailed structural representations for a CMAS glass. The generated structures are not only thermodynamically favorable (according to DFT calculations) but also agree with experiments (including our x-ray and neutron total scattering data as well as literature data). Detailed analysis of the final structure (including partial pair distribution functions, coordination number, and oxygen environment) enabled existing discrepancies in the literature to be reconciled and has revealed important structural information on the CMAS glass, specifically (i) the unambiguous assignment of medium-range atomic ordering, (ii) the preferential role of Ca atoms as charge compensators and Mg atoms as network modifiers, (iii) the proximity of Mg atoms to free oxygen sites, and (iv) clustering of Mg atoms. Electronic property calculations suggest higher reactivity for Ca atoms as compared with Mg atoms, and that the reactivity of oxygen atoms varies considerably depending on their local bonding environment. Overall, this information may enhance our mechanistic understanding on CMAS glass dissolution behavior in the future, including dissolution-related mechanisms occurring during the formation of low-CO₂ cements.

DOI: 10.1103/PhysRevMaterials.5.015603

I. INTRODUCTION

The structure and properties of silicate glasses are of significant interest to many scientific and technological fields such as condensed matter physics, geology, glass science, materials chemistry, energy, medicine, and advanced communication systems [1,2]. In particular, CaO-Al₂O₃-SiO₂ (CAS) ternary glasses are one of the most studied glass systems due to their advantageous optical, mechanical, and chemical properties [3–5], rendering them an attractive option for a wide range of applications such as nuclear waste encapsulation, high performance glasses, ceramics, metallurgical processes, and cements [6]. The structure of a CAS glass generally consists of silicate and aluminate tetrahedra (commonly referred as network formers) connected via their bridging oxygen (BO) atoms to form a network, which is modified by calcium cations (network modifiers). The impact of calcium on the aluminosilicate network structure is twofold: (i) to charge-balance the negative charge associated with aluminate tetrahedra (i.e., AlO₂⁻), and (ii) to break the aluminosilicate network creating nonbridging oxygen (NBO) atoms. The introduction of network modifiers (e.g., Ca) alters the structural properties of aluminosilicate glasses (e.g., relative amounts of BO and NBO) and consequently changes their physical.

optical, mechanical, thermal, and chemical properties [7–9].

Hence, the structural properties of ternary CAS glasses have

been widely studied both from an experimental [10-25] and

an impact on the aluminosilicate network structure similar

to calcium [34]. In fact, quaternary CaO-MgO-Al₂O₃-SiO₂

Magnesium is another common network modifier that has

computational [7,26–33] viewpoint.

use of OPC [43]. In addition, both CMAS slag and CAS

fly ash are important precursor materials for synthesis of

⁽CMAS) glasses are important constituents of the Earth's lower crust and mantle [34,35] and have industrial applications including metallurgical processes, concrete production, and emerging low-CO₂ cement technologies [36–43]. For instance, both CMAS (e.g., blast-furnace slag from steel manufacturing process) and CAS (e.g., coal-derived class C fly ash) glasses are often used to partially replace ordinary Portland cement (OPC) in concrete production to (i) enhance the mechanical properties and long-term durability of concrete and (ii) lower the CO₂ emissions associated with

alkali-activated materials (AAMs), which constitute a class of low-CO₂ cements with excellent mechanical, thermal, and chemical properties when properly formulated [42]. Both applications have great potential to significantly reduce the

^{*}Corresponding author: whitece@princeton.edu

environmental impact of the current cement industry, which accounts for 8–9% of global anthropogenic CO₂ emissions [44]. Furthermore, CMAS glass has been identified as a major source of corrosion and premature failure for ceramic thermal barrier coatings used to enhance the high-temperature behavior of alloys in spacecraft and aircraft [45,46].

To fully harness the benefits of CMAS glasses in these applications, it is critical to develop the composition-structureproperty relationships for the CMAS glass systems, and this necessitates the development of detailed realistic atomic structural representations. Computational tools such as ab initio and force-field molecular dynamics (MD) simulations have been used to predict glass structures, uncovering important structural details that are difficult to obtain solely with experiments. Specifically, force-field MD simulations have been widely used to predict the structure and properties of various silicate glasses and melts, including CAS [7,27,28,30–33,47] and CMAS [37,48–52] glass systems. A key advantage of force-field MD simulations compared with those based on ab initio MD is their relatively high computational efficiency, however, the accuracy of these simulations is highly dependent on the accuracy of the chosen force field for the material in question [31], where the force field is developed typically by refining the force-field parameters against limited experimental data and/or *ab initio* calculations [53]. Alternatively, a glass structure can be generated using ab initio MD in a more accurate and less biased manner, where the electronic structure calculations based on the Schrödinger equation are used instead of force fields. However, one major drawback of ab initio MD is its high computational demand that limits its application to relatively small systems and short simulation time for the modeling of silicate glasses [26,29,54–58], as compared to MD simulations. Studies have shown that modeling of silicate glass structures based on small systems (e.g., \sim 100 atoms) exhibits strong finite size effects on the structural properties (e.g., radial distribution functions and bond-angle distributions) [26,27].

In this study, we have combined force-field MD simulations with ab initio based density functional theory (DFT) calculations to generate realistic structural representations for a quaternary CMAS glass. This protocol involved subjecting five randomly generated structures (each with 439 atoms) to a melt-quench process using force-field MD simulations (widely used for modeling of silicate glass structure [37,59,60]) to obtain ten amorphous starting structural representations for the CMAS glass. The NVT ensemble was used for the melt-quench process where the density of the cell was adjusted accordingly and cooling rates of 0.57-1 K/ps were adopted. These structures were subsequently geometryoptimized using DFT calculations to further improve the accuracy of the structural representations. X-ray and neutron total scattering data were collected on an amorphous blastfurnace slag with the same CMAS composition to ensure that the DFT-optimized structures capture the short- and mediumrange ordering in the CMAS glass. We then thoroughly analyzed the structural properties of the ten final structural representations and compared with literature data, where important structural information on the CMAS glass has been uncovered. Specifically, key attributes that are computed and compared include the partial pair distribution functions, coordination numbers, oxygen environments, and distribution of the network modifiers around oxygen species. Finally, we calculated the electronic properties of the CMAS glass based on one DFT-optimized structure to evaluate the potential reactive sites. Overall, this study highlights the power of combining force-field MD simulations and DFT calculations to generate realistic structural representations for a CMAS glass. The generation of realistic structural representations will be particularly helpful for further developing our understanding of dissolution kinetics and mechanisms of CMAS glasses (and other types glasses) in aqueous environments when combined with experimental techniques such as *in situ* pair distribution function (PDF) analysis.

II. METHODS

A. Experimental details

A quaternary CMAS glass powder with a chemical composition of 42.3 wt % CaO, 32.3 wt % SiO₂, 13.3 wt % Al₂O₃, and 5.2 wt % MgO (the Australia slag in Ref. [36], measured using x-ray fluorescence) is used in this investigation. This slag sample is a commercial byproduct from a steel manufacturing plant produced by rapid quenching of molten slag often using jet water stream to retain a glassy state. This sample also contains trace amounts of other oxides, e.g., SO₃ (2.86 wt %), Fe₂O₃ (0.6 wt %), TiO₂ (0.49 wt %), K₂O (0.33 wt %). However, these trace oxides were not included in the simulations because (i) their molar percentages are much smaller than the four main oxides (i.e., CaO, SiO2, Al2O3, and MgO), and (ii) most sulfur in blast-furnace slag (CMAS glass powder used here) exists in sulfides [61], meaning that S incorporation into the glass phase is limited. Hence, only CaO, SiO₂, Al₂O₃, and MgO were included in the simulation of the glass structure. This CMAS glass has a similar chemical composition to a glass structure reported in the literature that was produced using force-field MD [52].

X-ray total scattering data were collected on the sample at room temperature on the 11-ID-B beam line at the Advanced Photon Source, Argonne National Laboratory, using a wavelength of 0.2114 Å and a Perkin-Elmer amorphous silicon two-dimensional image plate detector [62]. The wavelength was selected to provide a compromise between high flux (statistics), Q resolution, and a sufficient maximum momentum transfer. The sample was measured in a 1-mm-diameter polyimide capillary. The program FIT2D [63,64] was used to convert data from two dimensions to one dimension with CeO_2 as the calibration material. The PDF, G(r), is calculated by taking a sine Fourier transform of the measured total scattering function S(Q), where Q is the momentum transfer, as outlined by Egami and Billinge [65]. The x-ray PDF data were obtained using PDFgetX2 [66], with a Q_{max} of $20 \,\text{Å}^{-1}$. The instrument parameters ($Q_{\text{broad}} = 0.016 \,\text{Å}^{-1}$ and $Q_{\text{damp}} = 0.035 \,\text{Å}^{-1}$) were obtained by using nickel (a standard calibration material) and the refinement program PDFgui [67].

Neutron total scattering data were collected on the NPDF instrument at the Lujan Neutron Scattering Center, Los Alamos National Laboratory [68]. The sample was loaded in a vanadium can and measured for 8 hours at room temperature. Standard data reduction for generation of the neutron PDF was performed using the PDFgetN software [69], including a

background subtraction to remove incoherent scattering [70]. A $Q_{\rm max}$ value of $20\,{\rm \AA}^{-1}$ was used to produce the PDF. The neutron instrument parameters were produced using a silicon calibration material ($Q_{\rm broad} = 0.00201\,{\rm \AA}^{-1}$ and $Q_{\rm damp} = 0.00623\,{\rm \AA}^{-1}$).

B. Computational methods

To generate detailed structural representations for the CMAS glass measured above, we performed force-field MD simulations followed by DFT geometry optimization on a periodic box consisting of 439 atoms. All force-field MD simulations were performed with the ATK-Forcefield module in the QuantumATK software package [71,72]. First, five random structures consisting of 439 atoms each with a chemical composition of $(CaO)_{82}(MgO)_{14}(Al_2O_3)_{14}(SiO_2)_{59}$ (similar chemical composition as the experimental sample discussed above) were generated in cubic unit cells. The size of the cell was selected based on two competing considerations: (i) a minimum of \sim 200 atoms are required to limit the artificial finite size effects on the structural properties of CAS glasses [27], and (ii) the prohibitive computational demand of a large system size for subsequent DFT calculations. The density of the unit cell was initially set at 2.40 g/cm³, which is the estimated density for the CMAS glass at a temperature of 5000 K (detailed calculations for this density estimate using a method outlined in Ref. [73] and justification of the approach are given in the Supplemental Material [74]). For all force-field MD simulations, the interatomic potential and parameters developed by Matsui for crystals and melts of the CaO-MgO-Al₂O₃-SiO₂ system were used [75].

Each random structure was first subjected to an MD simulation at 5000 K for 1 ns to ensure the loss of the memory of the initial configuration and to reach an equilibrated melt state. The melt was then quenched using MD from 5000 to 2000 K in 3 ns followed by equilibration at 2000 K for 1 ns, before being further quenched from 2000 to 300 K in 3 ns, followed with another 1 ns equilibration time at 300 K. We have checked to ensure that 1 ns at 2000 K is sufficient for the equilibration of even the slowest atoms in the system (i.e., Si and Al), with the results (e.g., mean square displacement) shown in Figs. S1 and S2 of the Supplemental Material. The MD cooling rates of 1.0 and 0.57 K/ps were used here because it has been shown for silicate glasses that the structural properties of the resulting glasses (especially short-range structural ordering, such as the PDFs, bond angles, and coordination numbers) are close to convergence at MD cooling rates lower than 1 K/ps [59,60]. The canonical NVT ensemble (with the Nosé Hoover thermostat) and a time step of 1 fs were used for all the MD simulation steps above, while the density of the unit cell volume was adjusted to numerically estimated values at the corresponding temperature (calculations shown in the Supplemental Material) at the start of each equilibration step. The NVT ensemble was selected (as opposed to the NPT ensemble, which has been used in previous MD simulations [31]) because we found that the *NPT* ensemble with the Matsui force field [75] overestimates the density of the structure by $\sim 5-7\%$. This overestimation of density using NPT has also been reported in a previous investigation using the same Matsui force field [31] and another commonly used force field for CMAS systems (e.g., Guillot [76]). Recently, a study on alkali aluminosilicate glasses [77] has explored the impact of force-field type on glass density and showed that the estimated densities with the NPT ensemble are up to $\sim 10\%$ different from the experimental values.

The density of the 300 K final MD structures ($2.87 \, \mathrm{g/cm^3}$) agrees with experimental data on CMAS glasses that have similar compositions [38,39]. The evolution of ground-state energy of one 300 K MD structure (using single point DFT energy calculation) as a function of cell volume (Fig. S3 in the Supplemental Material) further confirms that the estimated density is accurate. Two configurations during the last 500 ps of the MD equilibration step at 300 K (separated by 500 ps) were extracted, leading to a total of ten structures for subsequent DFT calculations. The final unit cells have dimensions of $\sim 18 \times 18 \times 18 \, \mathrm{\AA}^3$.

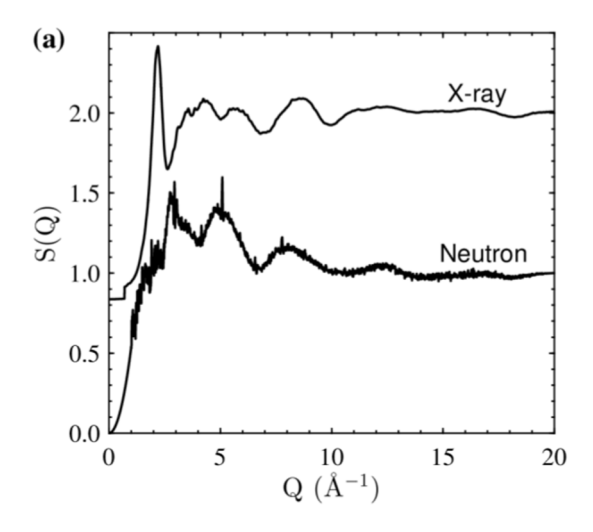
The configurations extracted from the MD simulations were then subjected to DFT geometry optimizations using the VASP software (version 5.4.1) [78]. The purpose of the DFT calculations was to further improve the chemical feasibility of the MD-generated structures. All DFT calculations were performed with the generalized gradient approximation-Perdew-Burke-Ernzerhof (PBE) exchange-correlation functional [using projector augmented wave (PAW) potentials] where the Brillouin zone was sampled using a $2 \times 2 \times 2$ Monkhorst-Pack mesh for k points. Atomic positions were optimized using the conjugate gradient method, where the total energy was minimized with the cell density fixed at 2.87 g/cm³. For the geometry optimization, a "low" precision was initially employed, where an energy convergence criterion of 10^{-2} eV (i.e., EDIFF in INCAR file) was adopted and a relatively large level of Gaussian smearing (0.2 eV width of smearing) was employed to aid convergence. The structure was further optimized using "low" precision without smearing before being subjected to another round of geometry optimization using the "accurate" setting, where the energy convergence criterion was 10^{-3} eV. A cutoff energy of 500 eV was used for the plane-wave basis set for all DFT calculations.

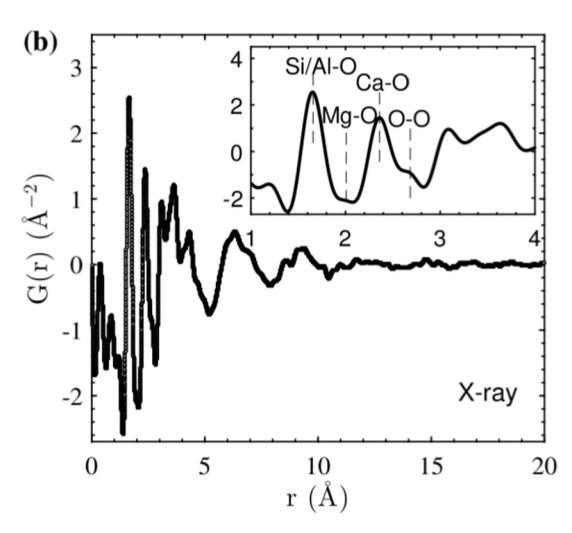
The simulated PDFs (both x-ray and neutron) of the final structural representations were produced using the PDFgui software [67]. The atomic displacement parameters were set at $u_{ii}^2 = 0.003 \, \text{Å}^2$, and the experimentally determined values for the Q-dependent instrument resolution ($Q_{\text{damp}} = 0.035$ and 0.00623 for x-ray and neutron data, respectively) and peak broadening ($Q_{\text{broad}} = 0.016$ and 0.00201 for x-ray and neutron data, respectively) parameters were used. The level of agreement between simulated and experimental PDFs was assessed in terms of the R_w value as defined in the PDFgui software [67], where a smaller R_w value implies better agreement. More details on the definition of R_w and the calculations of the simulated total and partial PDFs are given in the Supplemental Material.

III. RESULTS AND DISCUSSION

A. Experimental x-ray and neutron data

The experimental x-ray total scattering data for the CMAS glass powder are displayed in Fig. 1(a), which shows that this glass sample is predominately amorphous, as evidenced





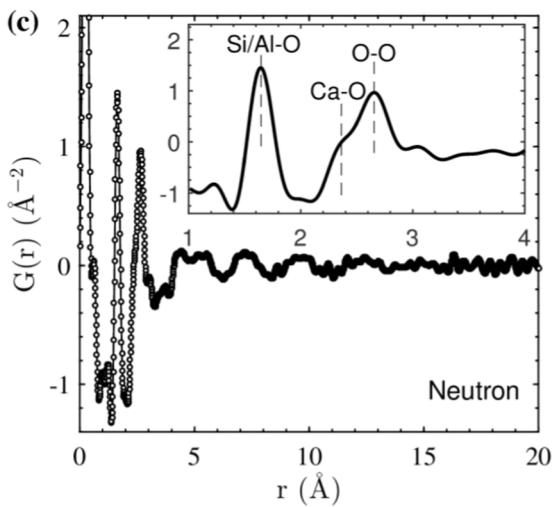


FIG. 1. (a) Stacked plot of the x-ray and neutron total scattering functions, (b) x-ray PDF, and (c) neutron PDF of the CMAS glass. Insets in (b) and (c) show a zoom of the PDF over an r range of 1--4 Å.

by the absence of any obvious Bragg peaks. The neutron total scattering data in Fig. 1(a), which were collected at a much higher Q resolution than the x-ray data, do exhibit several small Bragg peaks indicative of a very small crystalline

impurity. However, the contribution of the crystalline phase(s) to the atom-atom correlations in the PDF data is minimal, as evidenced by the lack of long-range ordering in both the x-ray and neutron PDFs displayed in Figs. 1(b) and 1(c), respectively. Furthermore, Figs. 1(b) and 1(c) show that the CMAS glass contains obvious short- ($<\sim$ 3 Å) and medium-range (\sim 3–10 Å) structural ordering, which is consistent with the structural features of silicate glasses [10,19,24,79,80]. Note that the peaks below $r\approx$ 1.4 Å in Figs. 1(b) and 1(c) are artifacts due to statistical noise, data termination errors, and imperfect corrections [65].

The nearest neighbor correlations at ~ 1.62 , ~ 2.00 , ~ 2.35 , and ~ 2.67 Å can be assigned unambiguously to Si/Al-O, Mg-O, Ca-O, and O-O correlations, respectively, based on literature data on aluminosilicate glasses [76]. However, assignment of the atomic correlations above ~ 3 Å for an amorphous material is difficult without an appropriate structural model (the structural representations generated in this investigation will be used to assign these atomic correlations later in the paper). It is noted that the x-ray and neutron data are complementary: the atom-atom correlations involving heavier elements (e.g., calcium-calcium and calcium-silicon) are more strongly weighted in the x-ray data than in the neutron data whereas correlations involving oxygen (e.g., oxygen-oxygen, calcium-oxygen, silicon-oxygen) dominate the neutron data due to its abundance in the sample (over 50%) along with its large neutron scattering length. Nevertheless, since the x-ray PDF data show more features compared with the neutron data, especially between 3 and 10 Å, the x-ray PDF data have been weighted more heavily when evaluating the level of agreement between the simulated data from the structural representation and the experimental PDF data.

B. Agreement between experiment and computation

Figures 2(a) and 2(b) display the comparisons between the experimental x-ray and neutron PDF data and the simulated x-ray and neutron PDFs obtained from a typical MD-generated initial structure and the corresponding DFT-optimized structure. The level of agreement achieved here for the DFT-optimized structure ($R_w \approx 0.35$) is better than our previous studies on the modeling of the atomic structure of amorphous magnesium carbonate ($R_w \approx 0.48$) [81] and metakaolin ($R_w \approx 0.77$) [82], and is comparable with several other studies on the modeling of the atomic structure of nanoparticles (e.g., gold nanoparticles, $R_w \approx 0.26$) [83] and amorphous solids (e.g., silicon [84] and graphene [85]).

It is clear that the structures generated here have captured the amorphous nature of the CMAS glass, specifically by the significant decrease in intensity beyond 4 Å for both the x-ray and neutron simulated PDFs [Figs. 2(a) and 2(b) and Fig. S4 in the Supplemental Material]. The structure also shows improved agreement with the x-ray experimental PDF data after undergoing the DFT calculation [Fig. 2(a)]. The R_w value is seen to decrease from 0.48 to 0.35, and the magnitude of reduction in R_w (i.e., the extent of improvement) is similar for all ten structural representations as shown in Figs. S4 and S5 in the Supplemental Material. Figure 2(a) and Fig. S4a (averaged over all the ten structural representations) show that the improved agreement after the DFT geometry

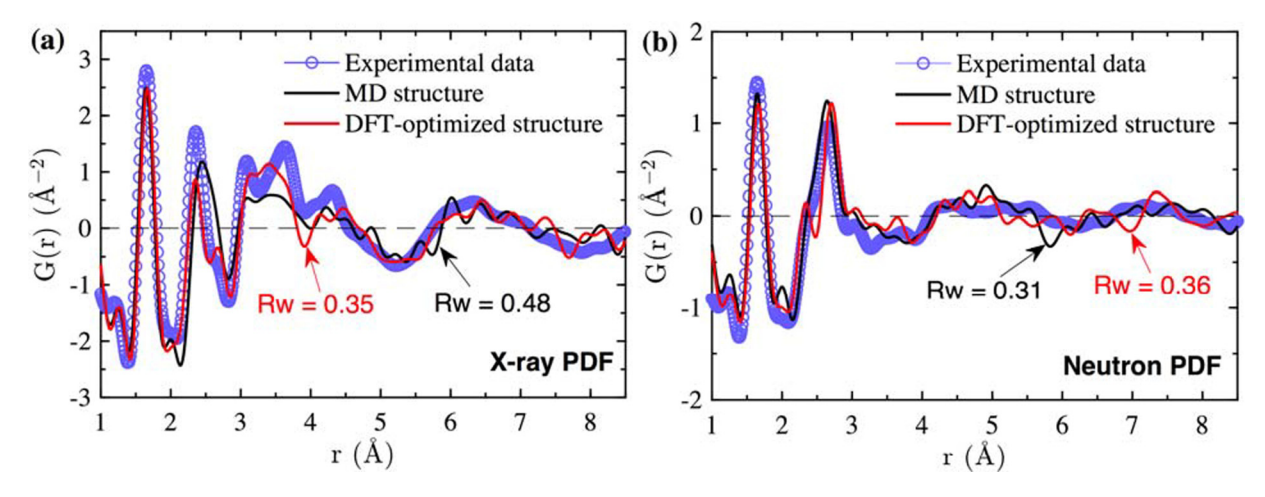


FIG. 2. Calculated (a) x-ray and (b) neutron PDFs from a force-field MD-generated CMAS glass structure and the subsequent DFT geometry-optimized structure, as compared with the experimental PDF data. Comparisons based on the average of all the ten structural representations are given in Figs. S4a and S4b in the Supplemental Material.

optimization is mainly attributed to (i) an improved fit of the nearest *X-X* correlations between 3 and 4 Å (X = Si, Al, Mg, and Ca; potential correlations include Si-Si, Si-Al, Al-Al, Ca-Si, Ca-Al, Ca-Mg, Ca-Ca, and Mg-Mg [52]), and (ii) a more accurate estimation of the Ca-O bond distance (i.e., ~ 2.35 Å as opposed to ~ 2.42 Å from MD simulations, as seen in Table I).

As further illustrated by the partial PDFs in Fig. 3 and Figs. S6 and S7 of the Supplemental Material, the improved agreement with the experimental data at \sim 3-4 Å is mainly attributed to the enhanced intensity of Ca-Ca and Ca-Si partial PDFs after DFT optimization. This enhanced intensity could be the result of the combined effect of the slightly altered (i) Ca-O distance in the first coordination shell (Table I), (ii) Ca-O-Si and Ca-O-Ca angular distributions (see Figs. S8h and S8j in the Supplemental Material), and (iii) coordination number distributions (see Fig. S9 and Table S1 in the Supplemental Material). In addition, DFT optimization is also seen to induce subtle improvement or changes to other local and medium range structural features including (i) the nearest interatomic X-O distances (Table I, and Fig. S6 and Table S2 of the Supplemental Material) and the second nearest interatomic X-O distances (Table S3 in the Supplemental Material), (ii) proportions of corner-, edge-, and face-sharing *X*-O-*X* configurations and interatomic *X*-*X* distances between connected polyhedra (Table S4 and Fig. S10 of the Supplemental Material), (iii) inter- and intrapolyhedra angular distributions (e.g., O-*X*-O and *X*-O-*X*; Fig. S8 of the Supplemental Material), and (iv) elimination/reduction of energetically less favorable coordination configurations (e.g., V-fold Si, VI-fold Al, and IV-fold Mg, see Table S1 of the Supplemental Material). Brief discussions of these detailed structural analysis results are also given in the Supplemental Material in the context of available literature data.

Overall, these results show that the DFT calculations lead to a better estimation of both the short- and medium-range atomic structure (specifically the level of agreement obtained with the x-ray PDF data) as compared with the MD-generated structure obtained using a commonly used force field for the CMAS system [75]. The neutron PDF data in Fig. 2(b) and Figs. S4b and S5 of the Supplemental Material, however, show a slight worsening of agreement (R_w increases from 0.31 to 0.36) after the DFT calculation. This is mainly attributed to a slight overestimation of the O-O distance in the DFT calculation (Table I), which has been strongly weighted in the neutron data. This agrees with previous DFT calculations

TABLE I. Comparison of MD and DFT predicted interatomic distances (averaged over ten structural configurations) with the experimental values reported for different silicate glasses. The values in the brackets are one standard deviation, based on the results from the ten structural representations.

| Nearest interatomic distance (Å) | MD | DFT | Experimental PDF data in this study | Experimental data in the literature | Difference ^c (%) | |
|----------------------------------|------------|------------|-------------------------------------|-------------------------------------|-----------------------------|--|
| Si-O | 1.63(0.00) | 1.64(0.00) | 1.64 ^a | ~1.61–1.64 [10,18,19,27,76] | 0 | |
| Al-O | 1.75(0.01) | 1.77(0.01) | N/A | ~1.74–1.77 [10,18,19,27,76] | 0.9 | |
| Mg-O | 2.03(0.02) | 2.02(0.02) | 2.00^{b} | $\sim 2.00 [76]$ | 1.0 | |
| Ca-O | 2.42(0.01) | 2.35(0.01) | 2.35 ^b | ~2.34–2.36 [10,18,19] | 0 | |
| 0-0 | 2.68(0.01) | 2.71(0.01) | 2.66 ^a | ~2.65–2.67 [19,76] | 1.9 | |

^aDerived from neutron PDF data.

^bDerived from x-ray PDF data.

^cRefers to the difference between the DFT-derived distance and the experimental data (literature data were used for the Al-O distance, as this information was not available from the x-ray or neutron experimental PDF data in this study).

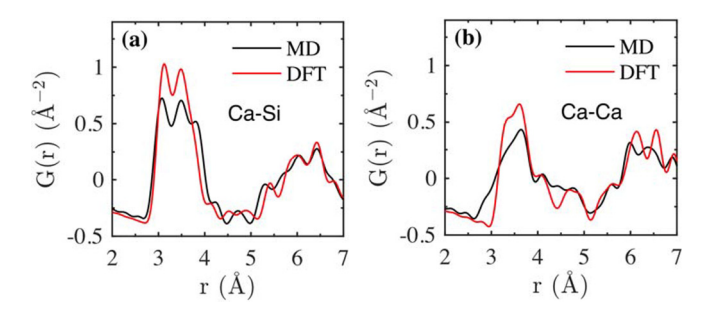


FIG. 3. Impact of DFT optimization on the partial x-ray PDF for (a) Ca-Si and (b) Ca-Ca pairs in the same structural representation used to produce the results in Fig. 2. Partial PDFs for a complete list of different atom-atom pairs in the same structural representations are shown in Fig. S6 in the Supplemental Material. Comparisons of the Ca-Si and Ca-Ca partial PDFs based on the average of all the ten structural representations are given in Figs. S7a and S7b in the Supplemental Material.

on silica glass in the literature where the PBE functional has been shown to give a slight overestimation of the O-O distance [57]. Nevertheless, all the nearest interatomic distances (including O-O distance) are less than 2% different from the experimental values (Table I), which is within the accuracy level of DFT calculations.

The differences seen between the experimental PDF and the simulated PDF from DFT-optimized structure could be attributed to a number of limitations of the current study, which include (i) finite size of the simulation cell, (ii) the rapid cooling rate adopted in the force-field MD simulations $(\sim 10^{12} \,\mathrm{K/s})$ used to prepare the initial amorphous structure as compared with that for typical experimental condition (1–100 K/s [60]), (iii) the presence of a small crystalline impurity and other trace elements (e.g., Fe, Ti, and S) that are not considered in the computation, and (iv) the limited ability of DFT geometry optimization to dramatically alter the glass structure (as compared to ab initio MD). The last aspect shows the need for future research using ab initio MD for further optimization of the structure, although ab initio MD is computationally more demanding and cannot always reproduce all structural features accurately. For example, an ab initio MD study [54] showed that the ab initio method underestimates the Si-O-Si/Al angles (compared to experimental data and force-field MD simulations) for natural silicate melts, partially due to the lack of description of long-range electron correlation in the study.

C. Analysis of the final structural representations

Figure 4(a) displays a typical final structural representation for the CMAS glass obtained after DFT geometry optimization, which clearly shows the amorphous nature of the structure. In general, the structure can be described largely as a depolymerized chainlike network structure consisting of corner-sharing SiO₄ and AlO₄ tetrahedra [86]. The aluminosilicate network in Fig. 4(b) reveals a considerable amount of Al-O-Al linkages, which will be quantified along with other structural features in the following subsections. Note that all the structural features and properties reported below are based

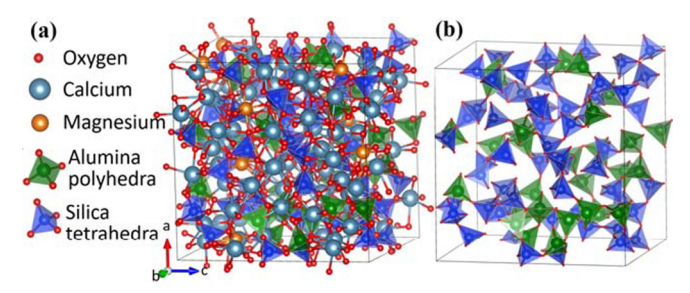


FIG. 4. (a) A representative final structure of the CMAS glass obtained after DFT geometry optimization. (b) The aluminosilicate network of the CMAS glass structure in (a).

on analysis of ten structural representations that have been geometry-optimized with DFT calculations.

1. Coordination states

The evolution of coordination number (CN) with increasing cutoff distance for the different atom-atom pairs is illustrated in Figs. 5(a) and 5(b). It is clear from Fig. 5(a) that the first coordination shells (involving oxygen atoms) of Si and Al are well defined since a plateau is reached for the CNs by 1.8 and 1.9 Å, respectively. The Si atoms are 100% tetrahedrally coordinated (see Table II) while Al atoms are seen to be dominated by tetrahedral coordination with a small proportion of V-fold coordination (\sim 3%), as shown in Table II (see Fig. S9a and Table S1 of the Supplemental Material for CN distribution of Si and Al atoms). For the CMAS glass investigated here, there are excess Ca and Mg atoms in the structure beyond those required to charge-balance the negative tetrahedral alumina sites, and therefore there should not be any V-fold Al atoms in the system based on simple stoichiometric considerations [22]. A previous NMR (²⁷Al) study on a CMAS glass with a similar chemical composition also suggested a single IV-fold coordination state for all Al atoms [86]. However, there are many MD simulations and experimental data (including ²⁷Al NMR) on peralkali/peralkaline-earth aluminosilicate glasses [e.g., Na₂O-Al₂O₃-SiO₂ [87], CAS [10–12,15,28,34], MgO-Al₂O₃-SiO₂ (MAS) [34,76,88,89], and CMAS [34,35]], where a small proportion of Al species with higher coordination states has been identified, in contrast to what is expected from consideration of the stoichiometry. In addition, it has been shown that cations with high field strength (e.g., Ca²⁺ and Mg²⁺) often lead to an increase in the amount of Al that has a CN above 4 (as compared to low field strength cations, e.g., Na^+ and K^+) [34,35] hence it is possible for V-fold Al to form in the CMAS glass studied here. It is noted that the limitations associated with the MD simulations (as discussed in Sec. III B) may have also contributed to the formation of V-fold Al.

In contrast with the evident cutoff distances for the average CNs of Si and Al atoms seen in Fig. 5(a), the CNs for Mg and Ca atoms (with oxygen) are highly dependent on the selected cutoff distance, which might contribute to the different oxygen CNs reported in the literature for Mg (~4–7 [76,90–92]) and Ca (~5–9 [10,16,34]) atoms in silicate glasses from simulations in comparison with experimental data. By using cutoff distances corresponding to the first minimum after

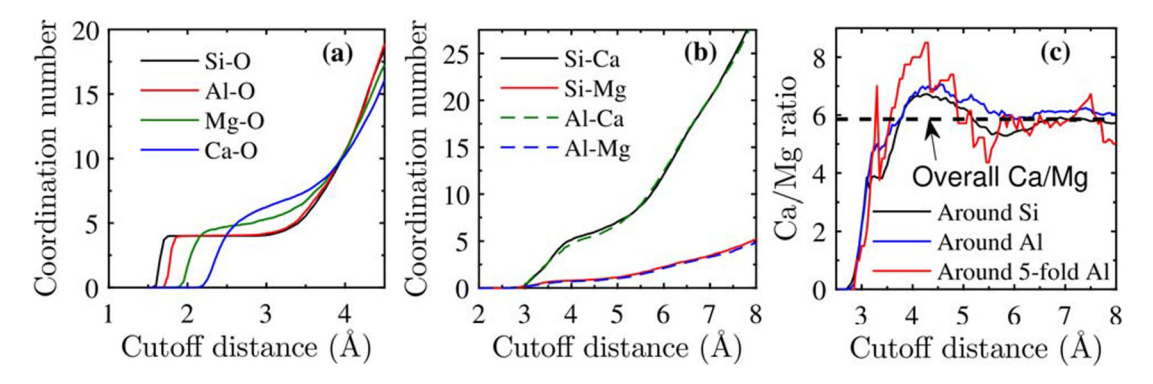


FIG. 5. Evolution of coordination number as a function of cutoff distance for (a) Si/Al/Mg/Ca-O (i.e., number of oxygen atoms surrounding Si, Al, Mg, Ca), (b) Si-Ca, Si-Mg, Al-Ca, and Al-Mg (i.e., number of Ca, Mg atoms surrounding Si, Al), and (c) Ca/Mg CN ratio around Si, Al, and fivefold Al atoms. The *y*-axis Ca/Mg ratio in (c) is calculated using the data in (b), for example, the Ca/Mg ratio around Si is determined by (Ca CN around Si)/(Mg CN around Si) at each given Ca/Mg-Si cutoff distance. Also given in (c) is the overall composition ratio of the system. The results are averages based on the ten structural representations optimized using DFT calculations.

the main peak of the partial PDFs, we see in Table II that the average CNs of Ca-O and Mg-O in the current work are approximately 6.73 and 5.15, respectively, which are in agreement with the previously reported values obtained using simulations and experiments (Table II). Even at these fixed cutoff distances (Table II), both Mg and Ca atoms have a distribution of oxygen CNs, as illustrated in Fig. S9b and Table S1 in the Supplemental Material. Figure S9b and Table S1 show that the Mg environment in the CMAS glass consists of four-, five-, six-, and sevenfold coordinated sites, with fivefold dominating as confirmed using x-ray absorption near-edge structure (XANES) [76,90] x-ray/neutron diffraction coupled with RMC refinement [76], and MD simulations [51]. Nevertheless, previous NMR (25Mg) studies on MAS and CMAS glasses show Mg is mainly in six coordination [86,92]. The discrepancy between different experimental results is partially attributed to the sensitivity of different experimental techniques to specific Mg bonding environments, as has been discussed in Ref. [93] for XANES and NMR.

The local coordination environment of the Ca atoms in the CMAS glass is dominated by six- and sevenfold coordinated Ca, along with the presence of five-, eight-, and ninefold coordination states (see Fig. S9b and Table S1 in the Supplemental Material for details). These results agree with previous experimental and MD studies where Ca has been shown to mainly reside in distorted sites with six to seven oxygen neighbors [10,16,34,52,86]. It is noted that literature data on alkaline-earth silicate glasses generally conclude that Ca atoms have higher CNs than Mg atoms within their first coordination shell, which is mainly attributed to the lower field strength (defined as Z/d^2 , where Z is the cation charge and d is the cation-oxygen distance) of Ca cation (\sim 0.36) as compared to Mg cation (\sim 0.46–0.53) [92].

To evaluate whether there is a preference for a specific network modifier (i.e., Ca and Mg) to charge-balance Al polyhedra, we have calculated the average number of Ca and Mg atoms around Si and Al atoms as a function of cutoff distance, as shown in Fig. 5(b). It is clear that the Ca (or Mg) CNs around Si and Al atoms are similar, indicating no obvious preference for Ca (or Mg) to associate with Si or Al atoms. The evolution of the (Ca CN)/(Mg CN) ratio around Si or Al as a function of the cutoff distance [Fig. 5(c)] shows that this ratio is slightly higher than the overall Ca/Mg compositional ratio (~5.9) of the CMAS glass at a cutoff distance of 4–5 Å, where the first coordination shells between the network formers and network modifiers are located. At the fixed cutoff

TABLE II. Coordination numbers at fixed cutoff distances for different atom-atom pairs. For an *X-Y* atom-atom pair, the coordination number of *X*, averaged over the ten DFT-optimized structural representations, is given, along with one standard variation shown in the brackets. Literature data on different types of silicate glasses (e.g., CAS [6,16], MAS [76,90] MS [92], CMAS [86], and NCAS [47]) are also given for comparison.

| | | | Literature data | | | |
|------------|------------------------|---------------|---|---|--|--|
| Atom pairs | Cutoff distance (Å) | Current study | Experiments (e.g., NMR [86,92], XANES [16,47,90], and neutron diffraction [6,10]) | Simulations (e.g., MD [6,52] and RMC + x-ray/neutron diffraction [76,91]) | | |
| Si-O | 2.2 | 4.00 (0.00) | 4 [86], 4.04 [10] | 4 [6,52,76] | | |
| Al-O | 2.5 | 4.03 (0.03) | 4 [86], 4.1–4.20 [6,10] | 4.0–4.10 [6,52] 4.1–4.16 [76] | | |
| Mg-O | 2.9 | 5.15 (0.15) | 5 [90], 6 [86,92] | 4.5 [91], 4.75–5.09 [76], 5.5 [52], 4.75–5.09 [76] | | |
| Ca-O | 3.2 | 6.73 (0.07) | 7 [47,86] 6–7 [16] | 6.00–6.24 [6], 6.7 [52], 7–7.5 [47] | | |
| Si-Ca | 4.5 | 5.96 (0.10) | N/A | 5.6 [52] | | |
| Si-Mg | 4.1 | 0.81 (0.03) | N/A | 3.5 [52] | | |
| Al-Ca | 4.5 | 5.58 (0.28) | N/A | 5.2 [52] | | |
| Al-Mg | 4.2 | 0.74 (0.20) | N/A | 1.4 [52] | | |

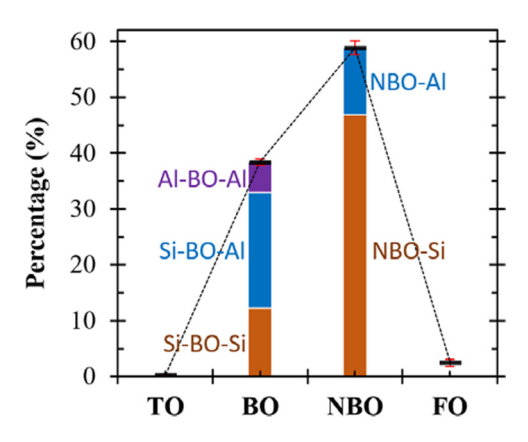


FIG. 6. Proportions of the different types of oxygen species. The total percentages of tricluster oxygen (TO), bridging oxygen (BO), nonbridging oxygen (NBO), and free oxygen (FO) are averages based on the ten DFT-optimized structural representations, with the red error bar indicating one standard deviation.

distances for each of the Ca/Mg-Si/Al pairs (as shown in Table II), we get a (Ca CN)/(Mg CN) ratio of \sim 7.4 and \sim 7.5 around Si and Al atoms, respectively. At a cutoff distance larger than 5–6 Å, the (Ca CN)/(Mg CN) ratio approaches the overall Ca/Mg ratio of the sample. These results indicate that there is a slight preference for Ca cation (over Mg) to associate with both types of network formers (i.e., Si and Al) within their first coordination shells, however, the Ca-Mg mixing around Al and Si atoms becomes completely random outside the first coordination shells. The same features are also seen around the fivefold Al site [as shown in Fig. 5(c)], which also suggests its slight preferential proximity with Ca (over Mg). The cause of this slight preferential proximity of Ca with Si, Al, and fivefold Al will be touched on in Sec. III C 3. It is noted that this observation is different from a previous MD investigation [52], which showed that the (Ca CN)/(Mg CN) ratios around Si (1.6) and Al (3.7) are significantly lower than the overall Ca/Mg compositional ratio of the CMAS glass in that study (4.4), indicating a preferential association of Mg with both Si and Al.

2. Oxygen environment

The oxygen environment, and in particular, the proportion of NBO species, has a large impact on glass properties (e.g., hardness [9], chemical reactivity [43], durability [8], and glass transition temperature [7]). Hence, we have calculated the proportion of different types of oxygen species based on the ten DFT-optimized structural representations and the results are

shown in Fig. 6. It is seen that the CMAS glass studied here has an NBO content of \sim 58.9% (percent relative to the total amount of oxygen atoms), which gives an NBO/T (T = Si or Al tetrahedra) of 1.75, a reflection of the degree of depolymerization of the glass structure. This indicates that this CMAS glass has, on average, a close to short-chain structure, which is consistent with NMR measurements on a CMAS glass of similar composition (with an average Q^n species of n = 2.2) [86]. Nevertheless, as shown in Table III, this percentage is slightly lower than the theoretical NBO content (\sim 64.6%) estimated using simple stoichiometry arguments [27] and assuming that the glass system consisted of perfect tetrahedra with only twofold oxygen atoms [i.e., no free oxygen (FO) that are not connected with any network formers or tricluster oxygen (TO) connected with three network formers]. Similar underestimation of the NBO content has been reported in a force-field MD study for CMAS melts with similar compositional ranges as the current study [51], nevertheless, studies on CAS glasses [21,28,29] have often exhibited higher NBO contents than the theoretical estimation. The discrepancy is mainly attributed to the fact that a small proportion of FO and TO species are regularly observed in aluminosilicate glasses [27,28,51,87], as also shown in the current study (Fig. 6), and their proportion varies considerably depending on the glass composition, although the limitations associated with the MD simulations (as discussed in Sec. III B) may have also contributed. The underestimation of the NBO percent in the current study is partially due to the relatively high proportion of FO ($\sim 2.5\%$, as compared to TO of $\sim 0.2\%$), arising from the relatively high modifier content (at ~50%, the amount of Ca and Mg relative to Ca, Mg, Si, and Al). In contrast, the CAS glasses in Refs. [21,28,29] have much higher proportions of TO (\sim 3– 7%) due to their relatively lower modifier content (\sim 10–30%) and/or higher Al/Si ratio (≫1), which may have led to the higher observed NBO content mentioned above (as compared to estimation from a simple stoichiometric argument).

The local environment surrounding the NBO sites has also been analyzed and reported in Fig. 6 and Table III, where it is seen that the proportion of NBO associated with Si atoms is about four times higher than that associated with Al atoms, in contrast with the overall Si/Al compositional ratio in the CMAS glass (i.e., 2.1 Si atoms for every Al atom). This suggests that there is a preferential formation of NBO around Si atoms and BO around Al atoms, which is consistent with previous studies on aluminosilicate glasses [14,16,17,28,35,76] where Al atoms are shown to prefer to reside in more polymerized environments than Si atoms. DFT calculations have shown that these preferential associations are mainly attributed to the higher energy penalty for the

TABLE III. Comparison of the proportions of different types of oxygen species [bridging oxygen (BO) and nonbridging oxygen (NBO)] between the structural representation in the current study and the theoretical estimation based on simple stoichiometric considerations and random mixing of network formers and oxygens (refer to the Supplemental Material for the calculations). The average values obtained for the ten structural representations are given along with one standard deviation.

| | | Percentage of different types of oxygen species (%) | | | | | | | |
|---|--------------------|---|--------------------|--------------------|--------------------|--------------------|------------------|--|--|
| | ВО | NBO | NBO-Si | NBO-Al | Si-BO-Si | Si-BO-Al | Al-BO-Al | | |
| Theoretical estimation Structural representations | 35.9 38.4 (0.5) | 64.1 58.9 (1.3) | 43.4 46.9 (2.1) | 20.6 12.0 (2.0) | 16.4 12.3 (1.1) | 15.9 20.7 (1.8) | 3.6 5.5 (1.4) | | |

formation of Al-NBO (108 kJ/mol) as compared to Si-NBO (72 kJ/mol) [13].

With respect to the BO sites, Fig. 6 shows that there is a small proportion of Al-BO-Al linkages, indicating that the Al-O-Al avoidance principle (Loewenstein's rule) prevalent in crystals is not fulfilled in this CMAS glass, as has been previously reported on aluminosilicate glasses, including simulations [27,28] and experiments [20,35]. Interestingly, the proportion of Al-BO-Al linkages (5.5%) is seen to be even higher than that estimated from a complete random distribution of Si and Al atoms around BO sites (3.6%, as shown in Table III; detailed calculations are shown in the Supplemental Material). This result indicates that the Al-O-Al avoidance principle is violated for this CMAS glass, which is different from several previous studies on NAS and CAS glasses, where the Al-O-Al avoidance principle is only partially violated [20,27]. The difference may be attributed to the higher proportions of strong modifier cations (Ca²⁺ and Mg²⁺) in the CMAS glass studied here (as compared to the NAS and CAS glasses in Refs. [20,27]), since the high field strength cations favor the negative charge concentration (e.g., Al-BO-Al) more than low-strength modifier cations (e.g., Na+) and hence promote the formation of Al-BO-Al linkages [20,21,88]. This is supported by another force-field MD study on CAS glasses, which showed that the proportion of Al-BO-Al sites becomes higher than theoretical values (assuming random distribution of Si and Al atoms around BO) when the Ca content reaches $\sim 50\%$ [28].

Finally, Table III shows that there is a preferential intermixing of Si-Al around BO, as evidenced by the higher proportion of Si-BO-Al (~20.7%) and lower proportion of Si-BO-Si $(\sim 12.3\%)$ linkages than the theoretical estimation based on random mixing of Si and Al (\sim 15.9 and \sim 16.4%). This preferential Si-Al intermixing is consistent with previous studies on aluminosilicate glasses where mixing between different network formers (as opposed to the same type of network formers) is preferred [35]. This is likely attributed to the often observed negative enthalpy of mixing between Al-rich and Al-poor glass, as has been shown in a solution calorimetry study on CMAS glasses [23,94]. Hence, the deviation from the theoretical proportions of oxygen species (Table III) is driven by two competing mechanisms: (i) strong modifier cations (i.e., Ca²⁺ and Mg²⁺) promote the formation of more negative BO sites (Al-O-Al > Si-O-Al > Si-O-Si) and (ii) negative enthalpy of mixing promotes intermixing of Si and Al atoms (Si-O-Al > Si-O-Si, Al-O-Al). The high proportion of Ca+Mg atoms in the CMAS glass (over 50%) renders mechanism (i) as the dominant mechanism, resulting in the larger proportion of Al-O-Al linkages than theoretically estimated. Both mechanisms (i) and (ii) favor formation of Si-O-Al over Si-O-Si, leading to the higher proportion of Si-O-Al and lower proportion of Si-O-Si than theoretical estimations (Table III).

3. Distribution of modifier cations around different oxygen species

Figure 7 shows the number of modifier cations (i.e., Ca and Mg) around the different types of oxygen species within their first coordination shell (based on analysis of the ten DFT-optimized structural representations), where the local Ca/Mg ratio around each type of oxygen species is compared with

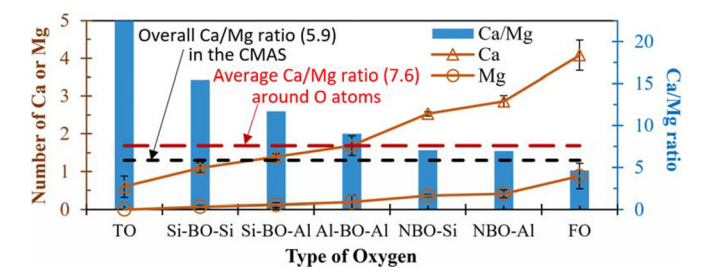


FIG. 7. Average number of Ca or Mg around each type of oxygen species, where TO, BO, NBO, and FO denote tricluster oxygen, bridging oxygen, nonbridging oxygen and free oxygen, respectively. The cutoff distances for Ca-O and Mg-O are fixed at 3.2 and 2.9 Å, respectively.

the average Ca/Mg ratio around O atoms (i.e., Ca/Mg of 7.6) and the overall Ca/Mg compositional ratio in the CMAS glass (i.e., Ca/Mg of 5.9). The difference between the two Ca/Mg ratios is attributed to the difference in the average oxygen CNs of Ca and Mg as seen in Table II $(7.6/5.9 = \sim 1.3 = 6.73/5.15)$. Given that the O-O distance has been slightly overestimated (i.e., $\sim 1.9\%$; Table I), we have evaluated the impact of lowering Si/Al/Mg/Ca-O cutoff distances by 2-3% in Fig. 7. The results are presented in Fig. S11 and Table S5 in the Supplemental Material, which closely resemble Fig. 7, with all the main features remaining the same.

In general, the average number of modifier cations (both Ca and Mg) increases as the number of network formers around the oxygen site decreases (i.e., number of modifier cations increases as transition from TO to BO, NBO, and FO sites). This is expected since more cations are required for charge-balancing as the oxygen sites become increasingly negative [e.g., $(FO)^{2-}$, $(Si_{1/4}\text{-NBO})^{-1}$, $(Al_{1/4}\text{-NBO})^{-5/4}$, $(Si_{1/4}\text{-BO-Si}_{1/4})^0$, $(Si_{1/4}\text{-BO-Al}_{1/4})^{-1/2}$]. Previous ^{17}O NMR measurements on CMAS glasses suggested a prevalence of 3Ca-NBO-Si around NBO-Si sites [23]. This suggestion is generally consistent with our results in Fig. 7, where an average of \sim 2.6 Ca atoms are seen around the NBO-Si sites with 3Ca-NBO-Si as the dominant species (see Fig. S12 in the Supplemental Material).

Furthermore, the Ca/Mg ratio around the oxygen site is seen to decrease as the oxygen site becomes increasingly negative (Fig. 7), which is attributed to the higher field strength of Mg (as compared to Ca), rendering it more effective in chargebalancing the more negative oxygen site. It is also seen that the Ca/Mg ratios around the three BO sites (\sim 9.0–15.5) are higher than the average Ca/Mg ratio around all O atoms (\sim 7.6), while the Ca/Mg ratios around the two NBO sites (\sim 7.0) are slightly lower than this average value. This result reveals a slight preference for Ca atoms to compensate charge and for Mg atoms to modify aluminosilicate network (creating NBO) in the CMAS glass, which is consistent with the observed preference of a high-field strength cation to associate with NBO for mixed alkali/alkaline earth glasses (e.g., preferential association of Ca with NBO for Ca-Na [47,95], and Mg with NBO for Mg-K [96]).

The lowest Ca/Mg ratio (\sim 4.6) is seen around the FO sites (Fig. 7), which are the most negative oxygen sites in the system [i.e., (FO)^{2–}], indicating a strong preferential association of FO sites with the Mg atom (as opposed to

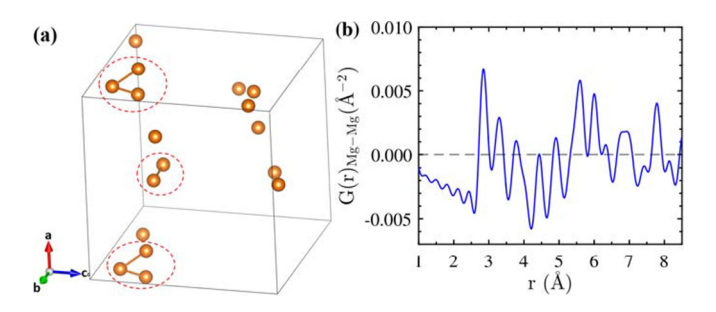


FIG. 8. (a) Small clusters of Mg atoms in a typical CMAS structural representation (several Mg atoms from adjecent cell are also shown), and (b) Mg-Mg partial x-ray PDF calculated using the ten final structural representations. For clarity, only Mg atoms are shown in (a) and Mg-Mg pairs with distance smaller than 3.5 Å are highlighted using red dashed circles.

Ca). Again, this preference is attributed to the higher field strength of Mg atom which enables it to more effectively charge-balance the highly concentrated negative charge surrounding FO sites. It has been previously shown that the FO content in CAS glasses with network-modifier molar contents of \sim 55–61% is around \sim 0.5–1.0% [28], which is much lower than the FO content in the current study (i.e., $\sim 2.3\%$), although the network-modifier content in the CMAS glass studied here is lower (\sim 50%). Moreover, a recent study on CAS and MAS melts (at 1773 K) showed that the MAS melt has a much higher FO content than the corresponding CAS melt for the same amount of modifiers (i.e., Mg or Ca) [48]. These results suggest that the presence of Mg in CMAS glass promotes the formation of FO, which is a contributing factor to the underestimation of the NBO content in the simulation as compared to the simple stoichiometric calculation (as shown in Table III). This preferential association of Mg atoms with FO sites also explains the higher Ca/Mg ratios around Si and Al atoms within their first coordination shell as compared to the average Ca/Mg compositional ratio in the CMAS glass [Fig. 5(c) and Table II].

Since FO sites are the most reactive oxygen sites, they are more prone to dissolve in aqueous solutions, which could be a major reason why CMAS glasses with higher Mg contents have been shown to exhibit higher reactivity [38,41,97]. Nevertheless, a carefully designed study is warranted to further confirm the positive correlation between Mg and FO content for CMAS glasses at room temperature. It is also noted that CMAS glass reactivity in an alkaline solution is highly complex and other factors, such as NBO content, particle size distribution, and thermal history of the CMAS glass can also have a large impact on its reactivity [43].

Finally, the deviation of the Ca/Mg ratios around the different oxygen sites from the average ratio indicates a nonrandom distribution of Ca-Mg around the oxygen sites with a slight degree of segregation (i.e., separate clustering of Ca and Mg atoms), which has been suggested for Ca-Mg around NBO sites in CMAS glasses according to an ¹⁷O NMR study [23]. The mild clustering of Mg atoms is indicated in Fig. 8(a), where a typical CMAS structural representation exhibits formation of small Mg clusters, with Mg-Mg pairs with distance smaller than 3.5 Å highlighted using red dashed circles. This is further supported by the Mg-Mg partial correlation aver-

aged over the ten final structural representation [Fig. 8(b)], which exhibits two peaks located at \sim 2.8 and 3.3 Å. These distances are much smaller than the theoretical distance of \sim 7.5 Å assuming a random distribution of Mg atoms in the unit cell, which is consistent with clustering of Mg atoms in the CMAS glass to a certain extent. However, further studies are required to confirm this Mg clustering in CMAS glasses.

In addition to the above structural analysis, we have also performed other detailed structural analyses for the DFT-optimized structural configurations, including bond angle distributions within polyhedra (O-X-O, Figs. S8a–S8d) and between different polyhedra (X-O-X, Figs. S8e–S8j), nearest neighbor Si/Al-BO/NBO distances, interatomic distances beyond the first coordination shell, and the proportions of corner-, edge-, and face-sharing configurations between different polyhedra (X-X, Table S4). These results along with brief discussions in the context of literature data are given in the Supplemental Material and further confirm that the final structures obtained using the MD-DFT method are realistic representations of the CMAS glass structure studied here.

4. Partial PDFs

The results presented in the previous sections show that the structural representations generated for the CMAS glass using the MD melt-quench process followed by DFT geometry optimization not only agree with our x-ray and neutron scattering data but also are generally consistent with literature data on aluminosilicate glasses, specifically in terms of interatomic distances, coordination numbers, and oxygen environments. With these realistic structural representations, it is now possible to unambiguously assign the features seen in the experimental PDF data [Figs. 1(b) and 1(c)], which would otherwise be an extremely challenging task to perform for the medium-range ordering (~3–8 Å) due to the overlapping nature of many individual atom-atom partials.

Figure 9 shows the partial x-ray PDFs based on the ten structural representations that have been subjected to DFT geometry optimization, as opposed to the partial x-ray PDFs in Fig. 3 and Fig. S6 of the Supplemental Material which are calculated based on one typical structural representation. It is clear that the medium-range ordering between \sim 4–5 Å is mainly attributed to the second nearest Si-O and Ca-O correlations in the CMAS glass, whereas the medium-range ordering between \sim 5–8 Å is mainly due to the third nearest Ca-O correlation and the second nearest Ca-Ca and Ca-Si correlations. Previously, the x-ray PDF peak located at \sim 3 Å for CMAS glasses has been assigned primarily to the nearest Si-Si/Al correlations based on partial radial distribution functions [36,52], however, Fig. 9 shows that this peak is dominated by the nearest Ca-Si/Al correlations with only minor contributions from the nearest Si/Al-Si/Al correlations. Another misassignment in Ref. [36] is the shoulder at \sim 3.3 Å [as seen in the inset figure in Fig. 1(b)], which was assigned to the nearest Mg-Si/Al correlations. However, Fig. 9 clearly shows that this shoulder is mainly attributed to the nearest Ca-Ca/Si correlations, with negligible contribution from Mg-Si/Al correlations.

In addition to the peak at \sim 3.1 Å, the nearest Ca-Si/Al correlations exhibit a second peak at \sim 3.6 Å. This double peak

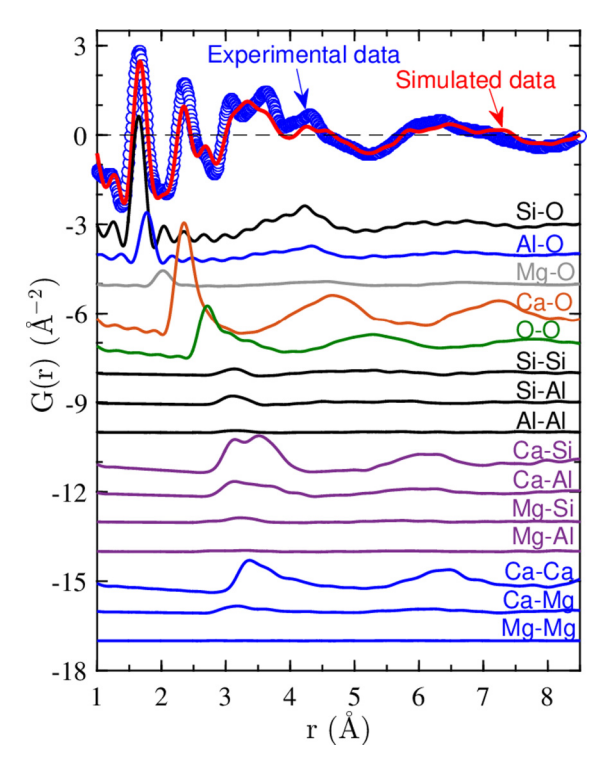


FIG. 9. Simulated partial x-ray PDFs based on the ten structural representations of the CMAS glass that have been geometry-optimized using DFT calculations.

feature for the nearest Ca-Si/Al correlations is commonly observed in CAS glasses [52], and is attributed to the connectivity between Si/Al tetrahedra and Ca polyhedra, where edge-sharing connectivity leads to the peak at \sim 2.8–3.1 Å and corner-sharing is responsible for the peak at \sim 3.3–3.6 Å. This is illustrated in Fig. S10 and Table S4 in the Supplemental Material, where it is clearly seen that the corner-sharing Ca-Si/Al distances are ~ 0.6 Å larger than that of the edgesharing Ca-Si/Al distances. A discussion of the proportion of corner-, edge-, and face-sharing X-X (X = Si, Al, Mg, and Ca) configurations and X-X distances (Fig. S10 and Table S4) in conjunction with bond angle distributions within polyhedra (O-X-O, Figs. S8a–S8d) and between different polyhedra (X-O-X, Figs. S8e-S8j), and calculated partial x-ray PDFs are also given in the Supplemental Material. The O-O partial PDF shows that the nearest O-O correlation exhibits two shoulders at \sim 3.0 and \sim 3.4 Å, in addition to the main peak at \sim 2.7 Å. Calculation of the O-O distances in all the Si/Al tetrahedra and Mg/Ca polyhedra (see Fig. S13 in the Supplemental Material) reveals that the main peak at \sim 2.7 Å is mainly attributed to the O-O distances in Si tetrahedra whereas the shoulder at \sim 3.0 Å is dominated by O-O distances from Al tetrahedra and Ca polyhedra. The shoulder of the O-O partial PDF at \sim 3.4 Å is primarily attributed to O-O correlations in the Ca polyhedra.

5. Electronic properties

The electronic structure of one DFT-optimized structural representation has been analyzed, with the electron isosurface density plots of selected regions shown in Figs. 10(a) and 10(b). As shown in these figures, the electron cloud (denoted by the color yellow) is predominately concentrated

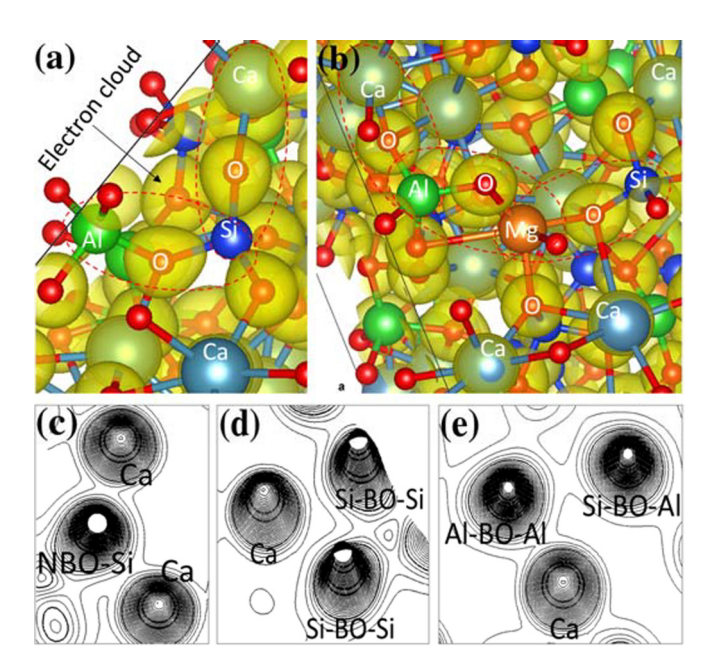


FIG. 10. (a),(b) 3D view of electron cloud density plots (denoted by the color yellow) around the different atoms with a threshold of $0.1\,\mathrm{eV/\mathring{A}^3}$ (a density lower than this value is not shown in the plots). Panels (c)–(e) show electron charge density contour plots on the plane passing through the selected atoms (as labeled in the plots). NBO-Si refers to nonbridging oxygen connected with a Si atom, whereas Si-BO-Si, Si-BO-Al, and Al-BO-Al refer to the three types of bridging oxygen.

around oxygen atoms while it is not visible around Si, Al, and Mg atoms at the selected threshold (i.e., 0.1 eV/Å^3). At this threshold, the electron cloud is clearly visible around the Ca atoms. We further quantified the electron charges around the different types of atoms using the commonly adopted Bader population analysis [98], which uses zero flux surfaces between different atoms to partition the electron density distribution for each atom [99]. The results are summarized in Table S6 of the Supplemental Material, which shows that the Bader effective charge of Ca atoms is around 6.464 electrons, much higher than those of Mg, Al, and Si atoms (0.338, 0.577, and 0.901 electrons, respectively). This effective charge value of Ca atoms is comparable to what was obtained in a previous DFT study on calcium aluminates using another analysis method (Mulliken [100]), i.e., \sim 6.7–6.9 electrons. The much higher effective charge around Ca atoms (as compared to the other network modifier, i.e., Mg atoms) is attributed to the higher activity of the six 3p electrons in the lower shell of Ca atoms (due to their relatively larger distances from the nucleus). This higher density of electrons near Ca (as compared to Mg) suggests that Ca sites have higher reactivity than Mg sites, which is consistent with literature data on Mg₂SiO₄ and Ca2SiO4 mineral dissolution, where the dissolution rate of calcium is several orders higher than magnesium [101].

As highlighted with the red dashed circles in Figs. 10(a) and 10(b), the shape of the electron cloud around the oxygen atom differs depending on the type of atoms bonded to the oxygen. Comparing the different X-O-X pairs reveals that the electron clouds are attracted toward the bonded atoms with a higher electronegativity value, with the following order: O

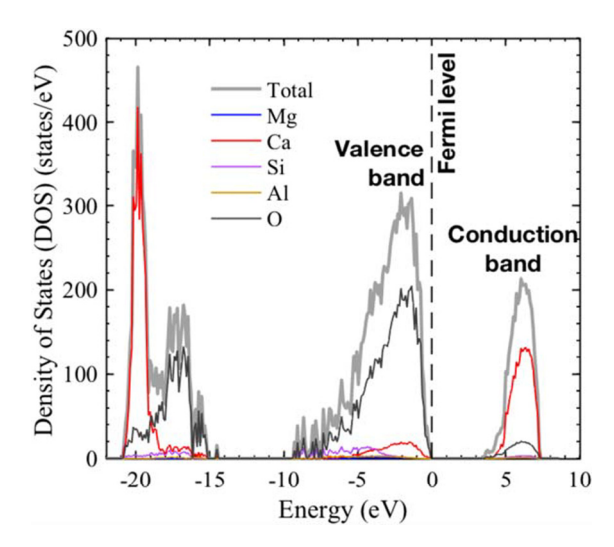


FIG. 11. Total electronic density of states (DOS) in states/eV for the DFT-optimized CMAS structure, along with the projected DOS contributions from each type of atom in the structure. All the energies are relative to the Fermi level set at the energy of 0 eV as shown by the dashed line.

> Si > Al > Mg > Ca (the corresponding electronegativity values are ~ 3.44 , ~ 1.90 , ~ 1.61 , ~ 1.31 , and ~ 1.00 , respectively, according to the Pauling scale [102]). Figures 10(c)-10(e) show the charge density contour plots for three selected atoms each calculated on the plane passing through these atoms (labeled in each figure). In each calculation, the same contour interval (0.1 eV/A^2) is used, with a darker and denser grid implying a higher electron density and stronger bonding, respectively. Hence, the slightly denser grid between Ca and NBO-Si (a similar contour plot for Ca and NBO-Al is shown in Fig. S14) than that between Ca and Si-BO-Si suggests that the Ca atom forms stronger bonds with NBO than Si-BO-Si. Comparing Figs. 10(d) and 10(e) suggests that the Ca atom forms stronger bonds with Al-BO-Al than Si-BO-Si. These results provide an indication of the relative strength of the different types of Ca-O bonds.

The total electronic density of states (DOS) of the DFToptimized CMAS glass structure along with the projected contribution from each type of atom are shown in Fig. 11. The calculated band gap (difference between the bottom of the conduction band and the top of the valence band) for this structure is about 3.2 eV, which is close to those obtained for a sodium silicate (\sim 3.2 eV) and a sodium calcium silicate glass $(\sim 3.4 \text{ eV})$ using DFT calculations [56]. Although it is known that DFT calculations performed using PBE functionals often underestimate the band gap, it is reliable and useful in comparing relative trends of calculated electronic properties [56]. Examining the DOS contribution from each type of atom reveals that the conduction band is dominated by Ca atoms with noticeable contribution from O atoms, while the valence band is dominated by O atoms with sizeable contribution from Ca atoms. This observation is consistent with Ref. [56]. The total DOS peak at \sim -20 eV is mainly attributed to Ca states while the peaks between \sim -15 and -18 eV are mainly due to O states. Since the top of the valence band and the bottom of the conduction band contains information on reactivity [103,104] the DOS data in Fig. 11 suggest that the reactivity of the CMAS glass is largely controlled by Ca and O atoms.

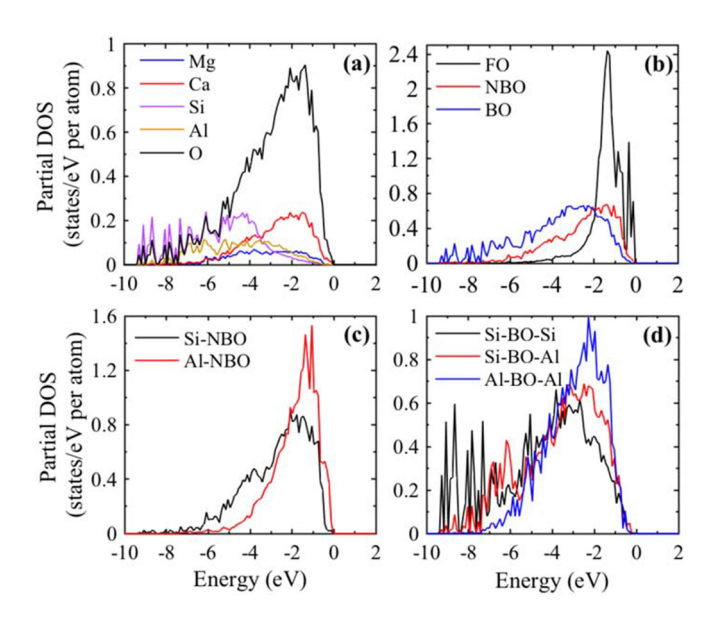


FIG. 12. Partial electronic density of states (DOS) in states/eV per atom for (a) each type of atom, and (b)–(d) different types of oxygen species. Panel (c) shows the two types of NBO bonded with either a Si or an Al atom, and (d) shows the three types of BO species.

Since electrons closer to the Fermi level have high potential to get involved in chemical reactions, the top of the valence band has a large impact on the reactivity of the system. Several previous DFT studies on tricalcium silicate and dicalcium silicate minerals [103,105] have shown that the top of the valence band is particularly informative on reactivity, and therefore we next focus on the comparison of the average DOS between different types of atoms near the Fermi level (e.g., between \sim -2 and 0 eV), as shown in Fig. 12(a). For this region, we clearly see that the DOS of Ca, Mg, Si, and Al atoms increases in the order of Si < Al < Mg < Ca, indicating an increase of reactivity in this order. This result is consistent with the known fact that the Si-O bond is harder to break than the Al-O bond, which is then stronger than Mg-O and Ca-O bonds [106]. In particular, the DOS of the Ca atom is substantially higher than the Mg atom in this region, indicating a higher reactivity for the Ca atom (as compared to Mg atom), which is consistent with the electron density results in Figs. 10(a), and 10(b) and literature data on Mg₂SiO₄ and Ca₂SiO₄ mineral dissolution rates [101].

The average DOS of the three types of oxygen species (i.e., FO, NBO, and BO) is given in Fig. 12(b), where we clearly see that the FO has the highest DOS near the Fermi level (e.g., between \sim -2 and 0 eV), followed by NBO and then BO. The observation that NBO has a higher DOS than BO close to the Fermi level is consistent with Ref. [56] on silicate glasses. This is also consistent with the DFT calculations in Ref. [105], where the DOS of the top of the valence band is located more around the FO sites in tricalcium silicate mineral (as opposed to NBO). This result suggests that the reactivity of oxygen species increases in the order of BO < NBO < FO, which is consistent with experimental data in the literature on silicate minerals dissolution [101], where a higher extent of depolymerization (increasing NBO) is often associated with higher dissolution rates. The DOS of the two types of NBO species and three types of BO species are compared in Figs. 12(c) and 12(d), respectively. Comparing the intensity of the DOS near the Fermi level suggests that NBO bonded with a Si atom has lower reactivity than that bonded with an Al atom and the reactivity of BO increases as the number of Al bonded with it increases. These results are also consistent with the fact that Al-O bond strength is lower than that of Si-O bond in aluminosilicates (hence easier to break) [106].

D. Broader implications and impact

CMAS glass reactivity is an important area of study, especially for sustainable cements, yet the exact impact of Ca, Mg, and Al content on the structure and properties of these CMAS glasses remains somewhat elusive. For example, several studies have shown that increasing Mg content generally leads to a higher reactivity for the CMAS glasses in an alkaline environment [97] and a higher strength for the final product [107]. However, in silicate mineral dissolution studies [101], it is generally shown that the dissolution of Ca is much faster than Mg. As discussed above, our electronic structure calculation results [Figs. 10(a), 10(b), and 12(a)] are consistent with the latter, where our results suggest that Ca exhibits higher reactivity than Mg. On the other hand, the structural analysis results in Fig. 7 show that the Mg atom exhibits a higher affinity with FO sites (as compared to Ca), which are the most reactive oxygen sites in the CMAS glass as evidenced by the DOS results in Fig. 12(b). It is likely that increasing Mg content (at fixed Si and Al content) would increase the formation of FO sites in CMAS glasses (as is shown to be the case in a recent force-field based MD simulation on CMAS glasses [48]) and hence lead to increase of reactivity. Due to the formation of FO sites in the CMAS glasses (not often formed in common silicate minerals), it is likely that both mechanisms are contributing to CMAS glass reactivity. However, it is noted that the reactivity of CMAS glasses is often highly complex in alkaline solutions, especially considering additional factors such as solution chemistry, particle size distribution, interaction between different network formers and modifiers, as well as the presence of minor oxides and crystalline impurities in the case of blast-furnace slags.

This study can be readily extended to cover a wider range of CMAS glass compositions to establish the important composition-structure-properties relationship for this important class of amorphous materials with broad scientific and industrial interest. Furthermore, with the generation of realistic structural representations, it becomes possible to unambiguously assign the medium-range ordering generally seen in the experimental PDF data of CMAS glasses and related amorphous materials. This information will be particularly useful when combined in the future with in situ PDF analysis to study amorphous-amorphous transformations, such as CMAS glass dissolution in aqueous environments, where changes to individual PDF peaks during the dissolution process can be directly related to the disappearance of certain structural features in the CMAS glass. The combination of glass structure modeling with in situ PDF analysis will be extremely helpful for studying the kinetics and mechanisms of glass dissolution, which is crucial for a range of industrially important processes, including bioglass dissolution, low-CO2 cements formation and degradation, glass corrosion, and nuclear waste encapsulation [43,108–110].

IV. CONCLUSIONS

In this study, we combined force-field molecular dynamics (MD) simulations with density functional theory (DFT) calculations to generate ten structural representations for a quaternary CaO-MgO-Al₂O₃-SiO₂ (CMAS) glass. Quantitative analysis of these ten structural representations showed that the CMAS glass structures generated using the method outlined in this study not only agree with our x-ray and neutron total scattering data but also are generally consistent with literature data on aluminosilicates with respect to interatomic distances, coordination numbers, oxygen environments, and angular distributions. Specifically, for the nearest-neighbor bonding environment with oxygen atoms Al is mainly in IV coordination with a small proportion of V-fold, whereas Ca and Mg atoms exhibit a much wider distribution of coordination states, with an average of \sim 6.73 and \sim 5.15, respectively. Analysis of the next nearest neighbors revealed that there is slight preference for Ca atoms (over Mg) to associate with both network formers (i.e., Si and Al atoms). Examination of the oxygen environment revealed several key features that are consistent with the literature, including violation of the Al-O-Al avoidance principle, preferential association of NBO with Si atoms (as opposed to Al atoms), and Si-Al intermixing. Calculation of the modifier environment around the different oxygen species showed a slight preference for Ca atoms to act as charge compensators and Mg atoms as network modifiers.

The results also revealed a preferential association of Mg with FO sites and a tendency for Mg to from small clusters in the CMAS glass. Given that FO sites are the most reactive oxygen sites [as evidenced by the electronic structure calculations, specifically a high density of states (DOS) near the Fermi level], this may help explain the higher reactivity of CMAS glass with higher Mg content when exposed to alkaline aqueous environments that has been observed in the literature. In contrast, the electronic structure calculations also suggest that the Ca atom exhibits higher reactivity than the Mg atom. This suggests that the impact of composition on the CMAS glass reactivity is highly complex. Hence, further studies on a wider compositional range of CMAS glasses are warranted to establish the important composition-structure and structure-properties relationships for these quaternary glass systems.

Finally, this investigation has enabled atom-atom correlations responsible for the medium-range ordering (\sim 3–8 Å) seen in the experimental PDF data of CMAS glass to be explicitly assigned. Correct assignment of these correlations in this region will not only enable better interpretation of existing PDF data but will also lead to advances in our understanding of dissolution mechanisms of CMAS glass (and related amorphous materials systems) in aqueous environments via experimental methods such as *in situ* PDF analysis.

ACKNOWLEDGMENTS

This material is based on work supported by the National Science Foundation (US) under Grant No. 1362039. The

DFT calculations were performed on computational resources supported by the Princeton Institute for Computational Science and Engineering (PICSciE) and the Office of Information Technology's High Performance Computing Center and Visualization Laboratory at Princeton University. The authors would like to acknowledge the support from the technical staff associated with the research computing facility at Princeton University. K.G. was partially supported by a Charlotte Elizabeth Proctor Fellowship from the Princeton Graduate School. The 11-ID-B beam line is located at

the Advanced Photon Source, an Office of Science User Facility operated for the US DOE Office of Science by Argonne National Laboratory, under US DOE Contract No. DE-AC02-06CH11357. The NPDF instrument is located at Los Alamos Neutron Science Center, previously funded by DOE Office of Basic Energy Sciences. Los Alamos National Laboratory is operated by Los Alamos National Security LLC under DOE Contract DE-AC52-06NA25396. The upgrade of NPDF was funded by the NSF through Grant No. DMR 00-76488.

- [1] E. Le Bourhis, *Glass: Mechanics and Technology*, 2nd ed. (John Wiley & Sons, Weinheim, 2014).
- [2] B. O. Mysen and P. Richet, Silicate Glasses and Melts, 2nd ed. (Elsevier, Amsterdam, 2018).
- [3] M. E. Lines, J. B. MacChesney, K. B. Lyons, A. J. Bruce, A. E. Miller, and K. Nassau, J. Non-Cryst. Solids 107, 251 (1989).
- [4] F. T. Wallenberger, R. J. Hicks, and A. T. Bierhals, J. Non-Cryst. Solids 349, 377 (2004).
- [5] A. Pönitzsch, M. Nofz, L. Wondraczek, and J. Deubener, J. Non-Cryst. Solids 434, 1 (2016).
- [6] N. Jakse, M. Bouhadja, J. Kozaily, J. W. E. Drewitt, L. Hennet, D. R. Neuville, H. E. Fischer, V. Cristiglio, and A. Pasturel, Appl. Phys. Lett. 101, 201903 (2012).
- [7] M. Bouhadja, N. Jakse, and A. Pasturel, J. Chem. Phys. 140, 234507 (2014).
- [8] B. C. Bunker, J. Non-Cryst. Solids 179, 300 (1994).
- [9] T. K. Bechgaard, A. Goel, R. E. Youngman, J. C. Mauro, S. J. Rzoska, M. Bockowski, L. R. Jensen, and M. M. Smedskjaer, J. Non-Cryst. Solids 441, 49 (2016).
- [10] L. Hennet, J. W. E. Drewitt, D. R. Neuville, V. Cristiglio, J. Kozaily, S. Brassamin, D. Zanghi, and H. E. Fischer, J. Non-Cryst. Solids 451, 89 (2016).
- [11] D. R. Neuville, L. Cormier, V. Montouillout, and D. Massiot, J. Non-Cryst. Solids 353, 180 (2007).
- [12] D. R. Neuville, L. Cormier, and D. Massiot, Chem. Geol. 229, 173 (2006).
- [13] S. K. Lee and J. F. Stebbins, Geochim. Cosmochim. Ac. 70, 4275 (2006).
- [14] L. Cormier, D. R. Neuville, and G. Calas, J. Am. Ceram. Soc. 88, 2292 (2005).
- [15] D. R. Neuville, L. Cormier, and D. Massiot, Geochim. Cosmochim. Acta 68, 5071 (2004).
- [16] D. R. Neuville, L. Cormier, A.-M. Flank, V. Briois, and D. Massiot, Chem. Geol. 213, 153 (2004).
- [17] J. R. Allwardt, S. K. Lee, and J. F. Stebbins, Am. Mineral. 88, 949 (2003).
- [18] V. Petkov, S. J. L. Billinge, S. D. Shastri, and B. Himmel, Phys. Rev. Lett. 85, 3436 (2000).
- [19] L. Cormier, D. R. Neuville, and G. Calas, J. Non-Cryst. Solids **274**, 110 (2000).
- [20] S. K. Lee and J. F. Stebbins, Am. Mineral. 84, 937 (1999).
- [21] J. F. Stebbins and Z. Xu, Nature (London) 390, 60 (1997).
- [22] S. Takahashi, D. R. Neuville, and H. Takebe, J. Non-Cryst. Solids **411**, 5 (2015).
- [23] S. Y. Park and S. K. Lee, Geochim. Cosmochim. Acta 80, 125 (2012).
- [24] M. Moesgaard, R. Keding, J. Skibsted, and Y. Yue, Chem. Mater. 22, 4471 (2010).

- [25] J. F. Stebbins, E. V. Dubinsky, K. Kanehashi, and K. E. Kelsey, Geochim. Cosmochim. Acta 72, 910 (2008).
- [26] P. Ganster, M. Benoit, J.-M. Delaye, and W. Kob, Mol. Simulat. 33, 1093 (2007).
- [27] P. Ganster, M. Benoit, W. Kob, and J.-M. Delaye, J. Chem. Phys. 120, 10172 (2004).
- [28] L. Cormier, D. Ghaleb, D. R. Neuville, J.-M. Delaye, and G. Calas, J. Non-Cryst. Solids **332**, 255 (2003).
- [29] M. Benoit, S. Ispas, and M. E. Tuckerman, Phys. Rev. B **64**, 224205 (2001).
- [30] H. Jabraoui, M. Badawi, S. Lebègue, and Y. Vaills, J. Non-Cryst. Solids 499, 142 (2018).
- [31] M. Bauchy, J. Chem. Phys. **141**, 024507 (2014).
- [32] M. Bouhadja, N. Jakse, and A. Pasturel, J. Chem. Phys. 138, 224510 (2013).
- [33] A. Tandia, N. T. Timofeev, J. C. Mauro, and K. D. Vargheese, J. Non-Cryst. Solids 357, 1780 (2011).
- [34] D. R. Neuville, L. Cormier, V. Montouillout, P. Florian, F. Millot, J.-C. Rifflet, and D. Massiot, Am. Mineral. 93, 1721 (2008).
- [35] S. K. Lee, G. D. Cody, and B. O. Mysen, Am. Mineral. 90, 1393 (2005).
- [36] K. Gong and C. E. White, Cem. Concr. Res. 89, 310 (2016).
- [37] C. Jiang, K. Li, J. Zhang, Q. Qin, Z. Liu, M. Sun, Z. Wang, and W. Liang, J. Non-Cryst. Solids **502**, 76 (2018).
- [38] M. Ben Haha, B. Lothenbach, G. Le Saout, and F. Winnefeld, Cem. Concr. Res. 41, 955 (2011).
- [39] M. Ben Haha, B. Lothenbach, G. Le Saout, and F. Winnefeld, Cem. Concr. Res. 42, 74 (2012).
- [40] S. A. Bernal, R. San Nicolas, R. J. Myers, R. M. de Gutiérrez, F. Puertas, J. S. J. van Deventer, and J. L. Provis, Cem. Concr. Res. 57, 33 (2014).
- [41] R. Snellings, T. Paulhiac, and K. Scrivener, Waste Biomass Valori. 5, 369 (2014).
- [42] J. L. Provis and J. S. J. van Deventer, *Alkali Activated Materials: State-of-the-Art Report*, RILEM TC 224-AAM (Springer/RILEM, Dordrecht, 2014).
- [43] J. Skibsted and R. Snellings, Cem. Concr. Res. **124**, 105799 (2019).
- [44] P. J. M. Monteiro, S. A. Miller, and A. Horvath, Nat. Mater. 16, 698 (2017).
- [45] S. Krämer, J. Yang, C. G. Levi, and C. A. Johnson, J. Am. Ceram. Soc. 89, 3167 (2006).
- [46] D. L. Poerschke, R. W. Jackson, and C. G. Levi, Annu. Rev. Mater. Res. 47, 297 (2017).
- [47] L. Cormier and D. R. Neuville, Chem. Geol. 213, 103 (2004).
- [48] C. Jiang, K. Li, J. Zhang, Q. Qin, Z. Liu, W. Liang, M. Sun, and Z. Wang, J. Mol. Liq. 268, 762 (2018).

- [49] C. Jiang, K. Li, J. Zhang, Q. Qin, Z. Liu, W. Liang, M. Sun, and Z. Wang, Metall. Mater. Trans. B **50**, 367 (2019).
- [50] D. Liang, Z. Yan, X. Lv, J. Zhang, and C. Bai, Metall. Mater. Trans. B 48, 573 (2017).
- [51] L. Mongalo, A. S. Lopis, and G. A. Venter, J. Non-Cryst. Solids 452, 194 (2016).
- [52] K. Shimoda and K. Saito, ISIJ Int. 47, 1275 (2007).
- [53] M. A. González, Ec. Themat. Soc. Fr. Ne. 12, 169 (2011).
- [54] R. Vuilleumier, N. Sator, and B. Guillot, Geochim. Cosmochim. Acta **73**, 6313 (2009).
- [55] K. Baral, A. Li, and W.-Y. Ching, AIP Adv. 9, 075218 (2019).
- [56] A. Tilocca and N. H. de Leeuw, J. Mater. Chem. 16, 1950 (2006).
- [57] C. Hühn, L. Wondraczek, and M. Sierka, Phys. Chem. Chem. Phys. 17, 27488 (2015).
- [58] K. Baral, A. Li, and W.-Y. Ching, J. Phys. Chem. A 121, 7697 (2017).
- [59] L. Deng and J. Du, J. Chem. Phys. 148, 024504 (2018).
- [60] X. Li, W. Song, K. Yang, N. M. A. Krishnan, B. Wang, M. M. Smedskjaer, J. C. Mauro, G. Sant, M. Balonis, and M. Bauchy, J. Chem. Phys. 147, 074501 (2017).
- [61] A. Roy, Cem. Concr. Res. 39, 659 (2009).
- [62] P. J. Chupas, K. W. Chapman, and P. L. Lee, J. Appl. Crystallogr. 40, 463 (2007).
- [63] A. P. Hammersley, S. O. Svensson, M. Hanfland, A. N. Fitch, and D. Hausermann, Int. J. High Pressure Res. 14, 235 (1996).
- [64] A. P. Hammersley, Report No. ESRF97HA02T, European Synchrotron Radiation Facility, 1997.
- [65] T. Egami and S. J. L. Billinge, Underneath the Bragg Peaks: Structural Analysis of Complex Materials (Pergamon, Elmsford, NY, 2003).
- [66] X. Qiu, J. W. Thompson, and S. J. L. Billinge, J. Appl. Crystallogr. 37, 678 (2004).
- [67] C. L. Farrow, P. Juhas, J. W. Liu, D. Bryndin, E. S. Božin, J. Bloch, T. Proffen, and S. J. L. Billinge, J. Phys.: Condens. Matter 19, 335219 (2007).
- [68] T. Proffen, T. Egami, S. J. L. Billinge, A. K. Cheetham, D. Louca, and J. B. Parise, Appl. Phys. A: Mater. 74, s163 (2002).
- [69] P. F. Peterson, M. Gutmann, T. Proffen, and S. J. L. Billinge, J. Appl. Crystallogr. 33, 1192 (2000).
- [70] K. Page, C. E. White, E. G. Estell, R. B. Neder, A. Llobet, and T. Proffen, J. Appl. Crystallogr. 44, 532 (2011).
- [71] QuantumATK version 2016.4, in *Synopsys QuantumATK* (Synopsys QuantumATK, Copenhagen, Denmarkc71, 2016), https://www.synopsys.com/silicon/quantumatk.html.
- [72] J. Schneider, J. Hamaekers, S. T. Chill, S. Smidstrup, J. Bulin, R. Thesen, A. Blom, and K. Stokbro, Model. Simul. Mater. Sci. 25, 085007 (2017).
- [73] K. C. Mills, L. Yuan, and R. T. Jones, J. S. Afr. I. Min. Metall. 111, 649 (2011).
- [74] See Supplemental Material at http://link.aps.org/supplemental/ 10.1103/PhysRevMaterials.5.015603 for more details on the MD simulations, calculation of PDFs, and analysis of the MDgenerated and DFT-optimized structures.
- [75] M. Matsui, Mineral. Mag. 58, 571 (1994).
- [76] M. Guignard and L. Cormier, Chem. Geol. 256, 111 (2008).
- [77] F. Lodesani, M. C. Menziani, H. Hijiya, Y. Takato, S. Urata, and A. Pedone, Sci. Rep. 10, 2906 (2020).

- [78] G. Kresse and J. Furthmüller, Phys. Rev. B 54, 11169 (1996).
- [79] R. N. Mead and G. Mountjoy, J. Phys. Chem. B 110, 14273 (2006).
- [80] P. H. Gaskell, M. C. Eckersley, A. C. Barnes, and P. Chieux, Nature (London) 350, 675 (1991).
- [81] C. E. White, N. J. Henson, L. L. Daemen, M. Hartl, and K. Page, Chem. Mater. 26, 2693 (2014).
- [82] C. E. White, J. L. Provis, T. Proffen, D. P. Riley, and J. S. J. van Deventer, Phys. Chem. Chem. Phys. **12**, 3239 (2010).
- [83] K. Page, T. Proffen, H. Terrones, M. Terrones, L. Lee, Y. Yang, S. Stemmer, R. Seshadri, and A. K. Cheetham, Chem. Phys. Lett. 393, 385 (2004).
- [84] A. Pandey, P. Biswas, B. Bhattarai, and D. A. Drabold, Phys. Rev. B 94, 235208 (2016).
- [85] B. Bhattarai, P. Biswas, R. Atta-Fynn, and D. A. Drabold, Phys. Chem. Chem. Phys. 20, 19546 (2018).
- [86] K. Shimoda, Y. Tobu, K. Kanehashi, T. Nemoto, and K. Saito, J. Non-Cryst. Solids 354, 1036 (2008).
- [87] M. Ren, J. Y. Cheng, S. P. Jaccani, S. Kapoor, R. E. Youngman, L. Huang, J. Du, and A. Goel, J. Non-Cryst. Solids 505, 144 (2019).
- [88] M. J. Toplis, S. C. Kohn, M. E. Smith, and I. J. F. Poplett, Am. Mineral. 85, 1556 (2000).
- [89] S. K. Lee, H.-I. Kim, E. J. Kim, K. Y. Mun, and S. Ryu, J. Phys. Chem. C 120, 737 (2015).
- [90] N. Trcera, D. Cabaret, S. Rossano, F. Farges, A.-M. Flank, and P. Lagarde, Phys. Chem. Miner. 36, 241 (2009).
- [91] L. Cormier and G. J. Cuello, Phys. Rev. B 83, 224204 (2011).
- [92] K. Shimoda, Y. Tobu, M. Hatakeyama, T. Nemoto, and K. Saito, Am. Mineral. 92, 695 (2007).
- [93] S. Kroeker and J. F. Stebbins, Am. Mineral. **85**, 1459 (2000).
- [94] A. Navrotsky, H. D. Zimmermann, and R. L. Hervig, Geochim. Cosmochim. Acta 47, 1535 (1983).
- [95] S. K. Lee and S. Sung, Chem. Geol. 256, 326 (2008).
- [96] J. R. Allwardt and J. F. Stebbins, Am. Mineral. 89, 777 (2004).
- [97] X. Ke, S. A. Bernal, and J. L. Provis, Cem. Concr. Res. **81**, 24 (2016).
- [98] R. Bader, Atoms in Molecules: A Quantum Theory (Oxford University Press, New York, 1990).
- [99] J. Du and L. R. Corrales, J. Chem. Phys. 125, 114702 (2006).
- [100] R. Mulliken, J. Chem. Phys. 23, 1841 (1955).
- [101] S. L. Brantley, in *Kinetics of Water-rock Interaction* (Springer, New York, 2008), pp.151–210.
- [102] L. C. Allen, J. Am. Ceram. Soc. 111, 9003 (1989).
- [103] Q. Wang, F. Li, X. Shen, W. Shi, X. Li, Y. Guo, S. Xiong, and Q. Zhu, Cem. Concr. Res. 57, 28 (2014).
- [104] V. O. Özçelik, K. Gong, and C. E. White, Nano Lett. **18**, 1786
- [105] E. Durgun, H. Manzano, R. Pellenq, and J. C. Grossman, Chem. Mater. 24, 1262 (2012).
- [106] K. H. Sun, J. Am. Ceram. Soc. 30, 277 (1947).
- [107] E. Douglas and J. Brandstetr, Cem. Concr. Res. **20**, 746 (1990).
- [108] G. S. Frankel, J. D. Vienna, J. Lian, J. R. Scully, S. Gin, J. V. Ryan, J. Wang, S. H. Kim, W. Windl, and J. Du, NPJ Mater. Degrad. 2, 15 (2018).
- [109] J. Du and J. M. Rimsza, NPJ Mater. Degrad. 1, 16 (2017).
- [110] A. E. Morandeau and C. E. White, Chem. Mater. **27**, 6625 (2015).